Journal of Computational Physics **176,** 145–169 (2002)
doi:10.1006/jcph.2001.6972, available online at http://www.idealibrary.com on IDEAL®

C^∞-Interpolation of Discrete Fields on Regular and Irregular Grids

Massimiliano Giona and Stefano Cerbelli

Dipartimento di Ingegneria Chimica, Università di Roma "La Sapienza," via Eudossiana 18, 00184 Rome, Italy
E-mail: max@giona.ing.uniroma1.it

Received April 9, 2001; revised October 15, 2001

The article proposes a simple C^∞ interpolation of discretized lattice fields on regular and irregular grids. The method is based on localized C^∞ but not analytic basis functions, which vanish outside an open set (region of influence). As a result, the interpolating fields at a point depend exclusively on the nodal values within the region of influence. The method can be applied to generic fields whose support is a limited set of n-dimensional space, starting from discretized values given on regular or irregular grids. Particular attention is focused on the interpolation of CFD-computed velocity fields that give rise to Lagrangian chaos. © 2002 Elsevier Science (USA)

Key Words: interpolation; C^∞ functions; Lagrangian analysis; fluid dynamics; laminar chaotic flows; mixing.

I. INTRODUCTION

A current issue in many engineering problems is the interpolation of a scalar or vector field with prescribed regularity constraints [1, 2]. These constraints, which may arise either from computational needs or physical conditions regarding the properties of the field, require that the interpolation be C^k $(k \geq 1)$, i.e., with continuous derivatives up to order k. For fluid dynamics applications, interpolation techniques are important both in solving the Navier–Stokes boundary value problem and in performing Lagrangian simulations of the dynamics of kinematic quantities associated with flow (particle and interface tracking).

Unchecked application of simple interpolation routines with limited regularity conditions may give rise to numerical inconsistencies and stability problems, especially in two- and three-dimensional simulations or in the presence of nonuniform grids.

A typical example where regularity conditions play a fundamental role is in stream-function/vorticity methods for two-dimensional flows [3]. Given the stream function ψ, obtained from computational fluid dynamics (CFD), the velocity field $\mathbf{v} = (v_x, v_y)^T$ is

0021-9991/02 $35.00

recovered from the first-order partial derivatives of ψ:

$$v_x = \frac{\partial \psi}{\partial y}, \quad v_y = -\frac{\partial \psi}{\partial x}. \tag{1}$$

From Eq. (1), it is clear that any interpolation of ψ should be at least C^1 in any open set embedded in the flow domain. The simplest and most widely used way to fulfill this requirement is to apply bicubic interpolation [4]. The use of this method requires that not only the values of ψ but also its first-order derivatives, $\partial\psi/\partial x$, $\partial\psi/\partial y$, and its second-order cross derivative, $\partial^2\psi/\partial x\partial y$, be specified at the nodes. In practice, these derivatives are obtained by discrete differentiation of the values of the function at the nodal points of the discrete grid. The accuracy of the resulting velocity fields obtained by interpolating the stream function therefore depends essentially on the accuracy in obtaining the required first- and second-order numerical derivatives at the nodes. As a result, the bicubic interpolation of ψ to obtain the velocity field corresponds to a C^0-interpolation of the velocity field itself obtained from discrete differentiation of the stream function. A review of several polynomial interpolation methods can be found in [5].

In addition to regularity conditions, other computational criteria related to algorithmic complexity (i.e., to the scaling of the computer time required to run an algorithm as a function of the number of grid nodes) may play a role in the choice of the most convenient interpolation strategy. Typical examples of techniques giving rise to such problems are Fourier series expansions (which are widely used for this purpose, especially in connection with spectral numerical methods, despite the fact that they cannot be strictly defined as interpolation but rather are L^2-approximations) and any kind of interpolation procedure for which the value at any point $\mathbf{x}$ is the weighted average of the interpolation basis functions $\phi_i(\mathbf{x})$ over all of the $N+1$ nodes of the discrete grid:

$$\psi_{\text{in}}(\mathbf{x}) = \sum_{i=0}^{N} a_i\, \phi_i(\mathbf{x}). \tag{2}$$

In these methods, the computation of the interpolating field at each point makes it necessary to sum over all of the $N+1$ interpolating functions. This nonlocal approach may be computationally unacceptable because of the huge amount of computer time needed to compute a sum over $N+1$ elements each time, especially in connection with Lagrangian simulations of particle tracking, which require the numerical integration of the velocity field in order to obtain the particle position. Since the integration of the kinematics equation of motion should be performed in Lagrangian simulations over long intervals of time and/or over a large number of particles in order to obtain statistically significant results (as required in order to obtain velocity correlation functions in turbulent flows [6, 7] or statistically relevant parameters such as the Lyapunov exponent or mixing efficiencies in laminar chaotic flows [8]), the extremely high number of calls to the interpolated velocity field in the presence of nonlocal interpolations may lead to unacceptably long computational times. This is, for example, the case with bicubic spline interpolation.

Recently, several nonlocal interpolation/approximation methods have been proposed based on the application of radial basis functions [9–11], on neural network approximation using sigmoidal functions [12–14], and on wavelet analysis [15–18]. The latter approach is grounded on multiresolution analysis [19] and reduces the interpolation problem to an iterative scheme by enforcing the ladder structure intrinsic to multiresolution decomposition.

This article proposes a simple and efficient local C^∞ interpolation scheme for approximating fields in an arbitrary number of dimensions ($D = 2, 3, \ldots$) starting exclusively from the values of the fields at the nodal points. The resulting interpolation function can be differentiated infinitely many times, and therefore[1] it is, *a fortiori*, C^1, as required in many applications. The interpolation scheme is formally analogous to Eq. (2) and can be defined in the classification adopted by Yeung and Pope [2] as an optimal interpolation. The central issue lies in the choice of the basis functions $\phi_i(\mathbf{x}) = \omega_i(\mathbf{x})$ (see Section II for their definition), which vanish outside a given neighborhood of the nodal point $\mathbf{x}_i$ (the region of influence). As a result, the interpolation is local in that the value at any point depends exclusively on the value at the grid points that fall within its region of influence. Since the number of nodes falling within the region of influence of any point is small and definitely much smaller than the total number of nodes, there are no computational problems related to nonlocal interpolations in connection with Lagrangian simulations.

Moreover, the interpolation procedure proposed requires only the nodal values of the field, provides accurate approximations for the first partial derivatives, and can be applied equally well on uniform and nonuniform (structured or unstructured) grids.

The article is organized as follows. Section II analyzes the properties of the localized basis functions $\omega_i(\mathbf{x})$. Section III develops the interpolation procedure and discusses the influence of the parameters on the accuracy. Section IV shows the numerical results obtained for model systems in one and two dimensions. Section V analyzes the results of the interpolation in the application to Lagrangian simulations of passive tracers in a model cavity flow giving rise to Lagrangian chaos.

II. LOCALIZED C^∞ BASIS FUNCTIONS

This section describes the main properties of the basis functions $\omega_i(x)$ used in the interpolation. We first consider the one-dimensional case. Let the family of functions $\omega_i(x) = \omega(x; x_i, \delta, \beta)$ on the real line $x \in (-\infty, \infty)$, depending on the parameters x_i, $\delta > 0$, $\beta > 0$, be given by

$$\omega(x; x_i, \delta, \beta) = \begin{cases} \exp\left[\beta + \frac{\beta\,\delta^2}{(x - x_i)^2 - \delta^2}\right], & x \in (x_i - \delta, x_i + \delta) \\ 0, & \text{elsewhere in } \Re. \end{cases} \tag{3}$$

The more compact notation $\omega_i(x) = \omega((x - x_i)/\delta)$ will be used in the rest of the article, omitting the explicit dependence on β and δ. The functions $\omega_i(x)$ defined by Eq. (3) are C^∞ but not analytic. The derivatives of any order of $\omega_i(x)$ can in fact be expressed as

$$\frac{p(x)}{[((x - x_i)^2 - \delta^2)^2]^m} \exp\left[\beta + \frac{\beta\,\delta^2}{(x - x_i)^2 - \delta^2}\right], \tag{4}$$

where m is a positive integer and $p(x)$ is a polynomial in x. For $x \to x_i \pm \delta$, the expression Eq. (4) tends to 0, which means that $\omega_i(x)$ can be differentiated infinitely many times over the real line. The function $\omega_i(x)$ is not, however, analytic in $(x_i - \delta, x_i + \delta)$ since it cannot be expressed as a Taylor series in the neighborhood of $x_i \pm \delta$. The localized C^∞ functions

[1] Given a bounded domain Q of $\Re^n$, the space of functions that are infinitely many times differentiable in Q, $C^\infty(Q)$ is defined as $C^\infty(Q) = \cap_{k=1}^{\infty} C^k(Q)$. Therefore, if $f \in C^\infty(Q)$, it follows that $f \in C^1(Q)$.

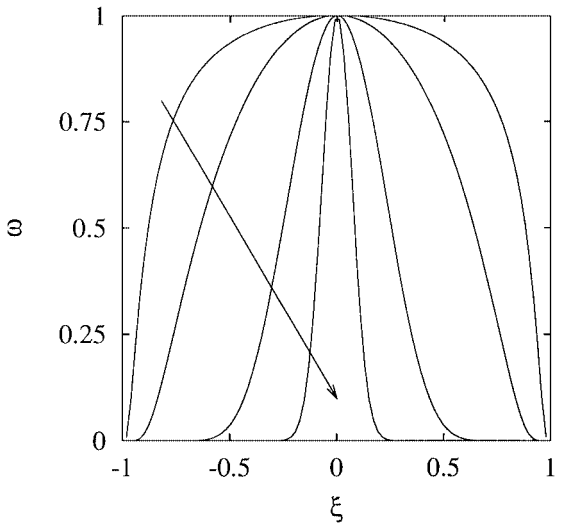

FIG. 1. $\omega(\xi)$ vs $\xi = (x - x_i)/\delta$ for several values of $\beta = 0.2$, 1, 10, 100. The arrow indicates increasing values of β.

$\omega_i(\mathbf{x})$ are widely used in functional analysis and in the theory of distributions (generalized functions). They are also applied as kernels to obtain regularized approximations of generalized functions and to prove density theorems for functional spaces (see, e.g., [20]).

As can be observed from its definition, Eq. (3), $\omega((x - x_i)/\delta)$ vanishes identically along with all of its derivatives outside the interval of width 2δ centered around x_i. Because of this property (which is particularly appealing for interpolation purposes), the functions $\omega((x - x_i)/\delta)$ are strongly localized[2], and the interval $(x_i - \delta, x_i + \delta)$ can be defined as their region (interval in the one-dimensional case) of influence. The region of influence $\mathcal{I}$ of a scalar function $f(\mathbf{x})$ is the set of points for which $f(\mathbf{x}) \neq 0$ (i.e., supp $(f) = \overline{\mathcal{I}}$).

Figure 1 shows the behavior of $\omega((x - x_i)/\delta)$ for several values of the parameter β. For $x = x_i$, $\omega((x - x_i)/\delta) = 1$ for all β. The parameter β plays the role of a localization parameter within the region of influence. As β increases, the functions $\omega((x - x_i)/\delta)$ are more peaked around $x = x_i$. We return to the influence of β in the analysis of the interpolation procedure.

There are several ways of defining localized C^∞ functions in $\Re^n$. Two of these are now explicitly discussed. The first way is to consider

$$\tilde{\omega}_i(\mathbf{x}) = \omega_i\left(\frac{|\mathbf{x} - \mathbf{x}_i|}{\delta}\right), \tag{5}$$

where $|\mathbf{x} - \mathbf{x}_i| = [\sum_{\alpha=1}^{n}(x_\alpha - x_{i,\alpha})^2]^{1/2}$ is the distance function in $\Re^n$. According to this definition, the region of influence is a ball of radius δ centered at $\mathbf{x}_i$. Alternatively, we can define a family of localized functions $\bar{\omega}_{i_1,\ldots,i_n}(\mathbf{x})$ on $\Re^n$ as

$$\bar{\omega}_{i_1,\ldots,i_n}(\mathbf{x}) = \prod_{\alpha=1}^{n} \omega\left(x_\alpha; x_{i_\alpha}, \delta_\alpha, \beta_\alpha\right), \tag{6}$$

[2] The concept of localization can be defined in terms of the region of influence. A function $f(\mathbf{x})$, $\mathbf{x} \in \Re^n$ is strongly localized if its region of influence (the closure of which is the support) is limited, i.e., is precompact.

centered at $\mathbf{x}_{i_1,\ldots,i_n} = (x_{i_1}, \ldots, x_{i_n})$, with $\delta_\alpha, \beta_\alpha > 0$, i.e., as the product of the n one-dimensional functions defined by Eq. (3) along each coordinate axis of a Cartesian reference system. In the case of Eq. (6), the region of influence is given by the rectangular set

$$\mathcal{I} = \{\mathbf{x} \mid |x_\alpha - x_{i,\alpha}| < \delta_\alpha, \alpha = 1, \ldots, n\}, \tag{7}$$

centered around $\mathbf{x}_{i_1,\ldots,i_n}$. The functions $\bar{\omega}_{i_1,\ldots,i_n}(\mathbf{x})$ defined by Eq. (6) possess more degrees of freedom (free parameters) than the functions $\tilde{\omega}_i(\mathbf{x})$ defined by Eq. (5). In the latter case, the region of influence is uniform with respect to all the coordinates and is characterized by the radius δ. The localization properties within the region of influence are enforced by means of a single parameter β. In the case of Eq. (6), the region of influence is specified by the widths δ_α of the n coordinate intervals, the Cartesian product of which forms $\mathcal{I}$. Moreover, a parameter β_α can be associated with each x_α. In principle, this gives much more flexibility in performing the interpolation. From now on, the basis functions $\bar{\omega}_{i_1,\ldots,i_n}(\mathbf{x})$ will be used, although qualitatively analogous results can be obtained by applying the functions defined by Eq. (5).

III. INTERPOLATION METHOD

This section analyzes the interpolation method based on the localized functions defined in Section II. The one-dimensional case of regular grids is first considered. The analysis is then extended to higher dimensions and nonuniform grids.

Let us consider an ensemble of grid points $x_i = i/N$, $i = 0, .., N$ on the unit interval [0, 1] (any bounded interval can be transformed upon rescaling into the unit interval). Let the values ψ_i of a continuous scalar field $\psi(x)$ be assigned. As for any optimal interpolation procedure, the interpolation writes

$$\psi_{\text{in}}(x) = \sum_{i=0}^{N} a_i \omega(x; x_i, \delta, \beta). \tag{8}$$

In Eq. (8) it is assumed that all of the interpolation basis functions are characterized by the same localization parameters δ and β.

The most naive interpolation strategy is to choose a region of influence of the basis function equal to the lattice spacing $\Delta x = 1/N$ between nodal points, $\delta = \Delta x$. As a result, since $\omega(x_k; x_i, \Delta x, \beta) = 0$, for $x_k \neq x_i$ and $\omega(x_i; x_i, \Delta x, \beta) = 1$, it follows immediately that $a_i = \psi_i$, $i = 0, \ldots, N$. While this approach yields a C^∞ interpolation for $\psi(x)$, it induces "unnaturally" constrained behavior for its derivatives. By the nature of the basis functions, any derivative of $\psi_{\text{in}}(x)$ of the order $k = 1, 2, ..$ is identically equal to 0 at the nodal points:

$$\left.\frac{d^k \psi_{\text{in}}(x)}{dx^k}\right|_{x=x_i} = 0, \quad i = 0, 1, \ldots, N. \tag{9}$$

In order to overcome this problem, the region of influence should be enlarged beyond the grid spacing, e.g., by choosing

$$\delta = (M + 1)\, \Delta x, \tag{10}$$

where M is a positive integer. The parameter M controls the number of basis functions that contribute to the value of the interpolating function at a generic node, which is at most equal to $2M+1$. Indeed, at any point $x \in [0,1]$, we have

$$\psi_{\text{in}}(x) = \sum_{i=[x]-M-1}^{[x]+M+1} a_i \omega_i(x), \tag{11}$$

where $[Nx]$ is the integer part of (Nx), and $a_i = 0$ for $i < 0$ and $i > N$. The values of the weights a_i $(i = 0, \ldots, N)$ can thus be obtained by solving the system of $N+1$ linear equations in the $N+1$ unknowns $\mathbf{a} = (a_0, \ldots, a_N)^T$ on obtained from Eq. (11) at $x = x_j$ $(j = 0, \ldots, N)$;

$$\mathbf{Ba} = (\mathbf{I} + \mathbf{\Omega})\mathbf{a} = \psi, \tag{12}$$

where $\mathbf{I}$ is the identity matrix, $\psi = (\psi_0, \ldots, \psi_N)^T$ is the vector of the nodal values of the function, and $\mathbf{\Omega} = \mathbf{B} - \mathbf{I}$ is the coefficient matrix.

Although not strictly necessary, it may be convenient to treat the interpolation of any point in a uniform way, i.e., such that the value of $\psi_{\text{in}}(x)$ at any $x \in [0,1]$ is always the sum of $2M+1$ contributions.

This leads to a discrimination among several interpolation strategies depending essentially on the way the endpoints of an interval are considered, as discussed below.

CASE I. Strict internal interpolation. In this approach, no external nodes are added, and the value of the interpolating function at $i = 0$ and $i = N$ is the sum of M contributions deriving from the internal nodes. In this case, the matrix $\mathbf{\Omega}$ attains the form

$$\mathbf{\Omega} = \begin{pmatrix} 0 & \hat{\omega}_1 & \hat{\omega}_2 & \hat{\omega}_3 & \cdots & \cdots & 0 & 0 & 0 \\ \hat{\omega}_1 & 0 & \hat{\omega}_1 & \hat{\omega}_2 & \cdots & \cdots & 0 & 0 & 0 \\ \hat{\omega}_2 & \hat{\omega}_1 & 0 & \hat{\omega}_1 & \cdots & \cdots & 0 & 0 & 0 \\ \cdot & \cdot & \cdot & \cdot & \cdots & \cdots & \cdot & \cdot & \cdot \\ 0 & \cdots & \hat{\omega}_2 & \hat{\omega}_1 & 0 & \hat{\omega}_1 & \hat{\omega}_2 & \cdots & 0 \\ \cdot & \cdot & \cdot & \cdot & \cdots & \cdots & \cdot & \cdot & \cdot \\ 0 & 0 & 0 & 0 & \cdots & \cdots & \hat{\omega}_1 & 0 & \hat{\omega}_1 \\ 0 & 0 & 0 & 0 & \cdots & \cdots & \hat{\omega}_2 & \hat{\omega}_1 & 0 \end{pmatrix}, \tag{13}$$

where the quantities $\hat{\omega}_i$ depend on β and M and are given by

$$\hat{\omega}_i = \exp\left[-\frac{\beta\, i^2}{(M+1)^2 - i^2}\right], \quad i = 1, \ldots, M. \tag{14}$$

The matrix $\mathbf{\Omega}$ is a Toeplitz matrix, characterized by the property that the entries along each diagonal are equal to each other [21].

CASE II. Periodic interpolation. This technique naturally applies in cases where the function $\psi(x)$ is periodic or can be made periodic. The abscissa x is no longer defined on the unit square but on the unit circumference S_1, and the distance between two points should therefore be defined by taking into account the compact topology of S_1. This can be straightforwardly taken into account by regarding the interpolation as if it were still on the

interval [0, 1] through the addition of M "fictitious" external nodes close to the endpoints, where periodic boundary conditions are enforced:

$$a_{-i} = a_{N-i}, \quad a_{N+i} = a_i, \quad i = 1, \ldots, M. \tag{15}$$

As a result, for the endpoint $j = 0$, the interpolation scheme leads to the equation

$$a_0 + \sum_{i=1}^{M} \hat{\omega}_i a_i + \sum_{i=1}^{M} \hat{\omega}_i a_{N-i} = \psi_0. \tag{16}$$

Since, due to the periodicity, $a_0 = a_N$, periodic interpolation leads to a system of N linear equations for the coefficients a_i ($i = 0, \ldots, N-1$), analogous to Eq. (12), with a coefficient matrix $\mathbf{\Omega}$ that is still Toeplitz and is given by

$$\mathbf{\Omega} = \begin{pmatrix} 0 & \hat{\omega}_1 & \hat{\omega}_2 & \hat{\omega}_3 & \cdots & \cdots & \hat{\omega}_3 & \hat{\omega}_2 & \hat{\omega}_1 \\ \hat{\omega}_1 & 0 & \hat{\omega}_1 & \hat{\omega}_2 & \cdots & \cdots & \hat{\omega}_4 & \hat{\omega}_3 & \hat{\omega}_2 \\ \hat{\omega}_2 & \hat{\omega}_1 & 0 & \hat{\omega}_1 & \cdots & \cdots & \hat{\omega}_5 & \hat{\omega}_4 & \hat{\omega}_3 \\ \cdot & \cdot & \cdot & \cdot & \cdots & \cdots & \cdot & \cdot & \cdot \\ 0 & \cdots & \hat{\omega}_2 & \hat{\omega}_1 & 0 & \hat{\omega}_1 & \hat{\omega}_2 & \cdots & 0 \\ \cdot & \cdot & \cdot & \cdot & \cdots & \cdots & \cdot & \cdot & \cdot \\ \hat{\omega}_2 & \hat{\omega}_3 & \hat{\omega}_4 & \hat{\omega}_5 & \cdots & \cdots & \hat{\omega}_1 & 0 & \hat{\omega}_1 \\ \hat{\omega}_1 & \hat{\omega}_2 & \hat{\omega}_3 & \hat{\omega}_4 & \cdots & \cdots & \hat{\omega}_2 & \hat{\omega}_1 & 0 \end{pmatrix}. \tag{17}$$

CASE III. External "flat" interpolation. The idea underlying this kind of interpolation is to introduce M external nodes close to the edges and to assume that

$$a_i = a_0, \quad a_{N+1} = a_N, \quad i = 1, \ldots, M, \tag{18}$$

i.e., that the coefficients associated to the external nodes "flatly" coincide with the coefficient at the closest end-node. For example, for $j = 0$, the interpolation scheme leads to the equation

$$a_0 + \left(\sum_{i=1}^{M} \hat{\omega}_i \right) a_0 + \sum_{i=1}^{M} \hat{\omega}_i \, a_i = \psi_0. \tag{19}$$

Eq. (12) is still valid, and the coefficient matrix Ω takes the form

$$\mathbf{\Omega} = \begin{pmatrix} \sum_{i=1}^{M} \hat{\omega}_i & \hat{\omega}_1 & \hat{\omega}_2 & \hat{\omega}_3 & \cdots & \cdots & 0 & 0 & 0 \\ \hat{\omega}_1 & \sum_{i=2}^{M} \hat{\omega}_i & \hat{\omega}_1 & \hat{\omega}_2 & \cdots & \cdots & 0 & 0 & 0 \\ \hat{\omega}_2 & \hat{\omega}_1 & \sum_{i=3}^{M} \hat{\omega}_i & \hat{\omega}_1 & \cdots & \cdots & 0 & 0 & 0 \\ \cdot & \cdot & \cdot & \cdot & \cdots & \cdots & \cdot & \cdot & \cdot \\ 0 & \cdots & \hat{\omega}_2 & \hat{\omega}_1 & 0 & \hat{\omega}_1 & \hat{\omega}_2 & \cdots & 0 \\ \cdot & \cdot & \cdot & \cdot & \cdots & \cdots & \cdot & \cdot & \cdot \\ 0 & 0 & 0 & 0 & \cdots & \cdots & \hat{\omega}_1 & \sum_{i=2}^{M} \hat{\omega}_i & \hat{\omega}_1 \\ 0 & 0 & 0 & 0 & \cdots & \cdots & \hat{\omega}_2 & \hat{\omega}_1 & \sum_{i=1}^{M} \hat{\omega}_i \end{pmatrix}. \tag{20}$$

These three variations on the theme lead to the same equation, Eq. (12), for determining the coefficient vector **a**, which can be expressed in the equivalent form

$$\mathbf{a} = L[\mathbf{a}] = -\mathbf{\Omega a} + \psi, \tag{21}$$

and they are suitable for unified mathematical treatment.

Eq. (21) can be viewed as the definition of the linear operator $L[\mathbf{a}]$ in the Euclidean $\Re_\infty^{N+1}$ space ($\Re_\infty^N$ for Case II, because of periodicity), equipped with the following metrics:

$$\rho_\infty(\mathbf{x}, \mathbf{y}) = \max_{0 \le i \le N} |x_i - y_i|. \tag{22}$$

The following Lemma holds.

LEMMA 1. *In the space $\Re_\infty^{N+1}$, the linear operator defined by Eq.* (21) *is a contraction if the condition*

$$\sum_{j=0}^{N} |\Omega_{ij}| \le \alpha < 1, \quad i = 0, 1, \ldots, N, \tag{23}$$

holds, where Ω_{ij} are the entries of the matrix $\mathbf{\Omega}$.

Proof. This is an elementary application of the Banach contraction theorem. The detailed proof can be found in [22]. ■

A simple application of Lemma 1 leads to the following result.[3]

THEOREM 1. *For any $M = 1, 2, \ldots$, there is a value $\beta^*(M)$ such that for $\beta > \beta^*(M)$ and for any interpolation scheme I–III adopted*:

- The operator $L[\mathbf{a}]$ is contractive;
- Eq. (12) admits a unique solution.

Proof. Consider the sum of the entries of the matrix $\mathbf{\Omega}$ over each row. Independently of the interpolation strategy adopted (Cases I–III), it follows that

$$\sum_{j=0}^{N} |\Omega_{ij}| \le 2 \sum_{j=1}^{M} \hat{\omega}_j(\beta, M) = 2 \sum_{i=1}^{M} \exp\left[-\frac{\beta i^2}{(M+1)^2 - i^2}\right] = \Phi(\beta, M). \tag{24}$$

For any fixed M, the function $\Phi(\beta, M)$ is continuous and decreases monotonically with β. Since $\Phi(0, M) = 2M$ and $\lim_{\beta \to \infty} \Phi(\beta, M) = 0$, there exists a value $\beta^* = \beta^*(M)$ such that $\Phi(\beta^*, M) = 1$. Therefore, for $\beta > \beta^*(M)$, $\Phi(\beta, M) = \alpha < 1$. By enforcing the result of Lemma 1, the first part of the theorem is proved. The second part follows from the Banach contraction theorem. Since $L[\mathbf{a}]$ is contractive, there exists a unique fixed point, say $\mathbf{a} = \mathbf{a}^*$, such that $\mathbf{a}^* = L[\mathbf{a}^*]$. By definition, $\mathbf{a}^*$ satisfies Eq. (12) and the proof is complete. ■

As a byproduct of Theorem 1, we obtain a straightforward iterative method for obtaining the interpolation coefficients **a**.

[3] The contractive nature of the operator L admits the practical implication that the coefficients of the C^∞ interpolation can be straightforwardly obtained by means of a simple and uniformly convergent iterative method, enforcing the Banach fixed-point theorem.

COROLLARY 1. *If $\beta > \beta^*(M)$, for any of the interpolation schemes considered, the iterative scheme*

$$\mathbf{a}^{(n+1)} = -\boldsymbol{\Omega}\mathbf{a}^{(n)} + \boldsymbol{\psi}, \quad n = 0, 1, \ldots \tag{25}$$

converges towards the solution of Eq. (12) *independently of the initial vector* $\mathbf{a}^{(0)}$.

It is important to observe that Theorem 1 does not imply that Eq. (12) admits no solution for $\beta \leq \beta^*(M)$. The statement of Theorem 1 is a sufficient condition providing a "safe" lower bound for the localization exponent that ensures the existence of the solution. It also yields an efficient iterative procedure for the numerical determination of the coefficient vector.

The extension to two-dimensional and higher dimensional problems is straightforward. We shall consider here the case of the basis functions $\bar{\omega}_{i_1,\ldots,i_n}(\mathbf{x})$ given by the product of the one-dimensional basis functions, in the case where the parameters δ_α, β_α ($\alpha = 1, 2, \ldots, n$) are the same and uniform for all the basis functions. In the case of a two-dimensional uniform grid $\mathbf{x}_{hk} = (h/N, k/N)$, $h, k = 0, \ldots, N$, the analog of Eq. (11) reads

$$\psi_{\text{in}}(\mathbf{x}) = \sum_{i=[x]-M-1}^{[x]+M+1} \sum_{j=[y]-M-1}^{[y]+M+1} a_{ij}\, \omega_i(x)\, \omega_j(y), \tag{26}$$

where $\mathbf{x} = (x, y)$, and the weights a_{ij} can be obtained by solving the corresponding linear problem analogous to Eq. (12).

THEOREM 2. *Consider a C^∞ interpolation scheme with respect to the functions $\bar{\omega}_{i_1,\ldots,i_n}$* (**x**) *given by Eq.* (6) *over an n-dimensional uniform grid. For any $n = 1, 2, \ldots$ and $M = 1, 2, \ldots$, the operator $L[\mathbf{a}]$ defined by the corresponding linear equation for the coefficients Eq.* (21) *is contractive for $\beta > \beta^*(M, n)$ where $\beta^* > 0$ is the unique solution of the equation*

$$[\Phi(\beta^*, M) + 1]^n = 2. \tag{27}$$

Proof. In the n-dimensional case, the matrix Ω is $(N+1)^n \times (N+1)^n$, and its entries can be labeled as $\Omega_{(i_1,\ldots,i_n)(j_1,\ldots,j_n)}$. Condition Eq. (23), ensuring the contractiveness of the operator $L[\mathbf{a}]$, becomes

$$\sum_{j_1,\ldots,j_n} \left|\Omega_{(i_1,\ldots,i_n)(j_1,\ldots,j_n)}\right| \leq \sum_{j_1=-M}^{M} \cdots \sum_{j_n=-M}^{M} \hat{\omega}_{j_1} \cdots \hat{\omega}_{j_n} - 1 = \left(\sum_{j=-M}^{M} \hat{\omega}_j\right)^n - 1$$
$$= [\phi(\beta, M) + 1]^n - 1 \leq \alpha < 1. \tag{28}$$

The threshold value $\beta^*(M, n)$ for the contractiveness of the operator $L[\mathbf{a}]$ is therefore the solution of Eq. (27). The remainder of the proof is identical to that of Theorem 1. ■

Figure 2 shows the behavior of $\beta^*(M, n)$ vs M for $n = 1, 2, 3$. The threshold value of β increases with M, as expected, because β and M counterbalance their action. A larger region of influence requires a stronger localization within it, i.e., a higher value of the localization exponent β. Moreover, β^* increases with the dimension n of the space n within which the data are embedded.

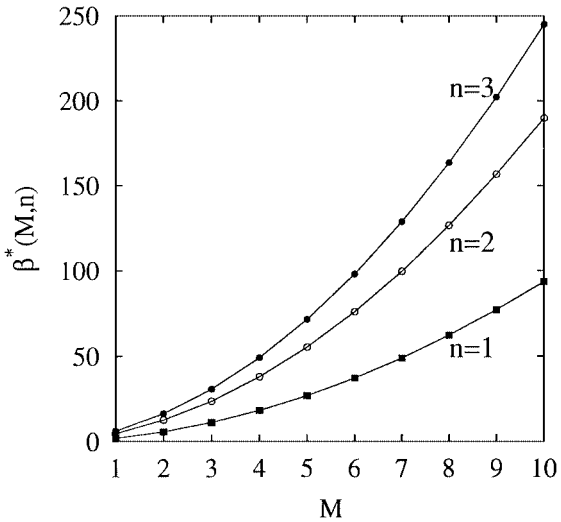

FIG. 2. $\beta^*(M, n)$ vs M for several values of the dimension n.

By the nature of the interpolation procedure, the extension to nonuniform grids is straightforward. Given the N nodal couples $(\mathbf{x}_i, \psi_i)$, where the nodal points are arbitrarily distributed, the interpolating function $\psi_{\text{in}}(\mathbf{x})$ is simply given by

$$\psi_{\text{in}}(\mathbf{x}) = \sum_{i=1}^{N} a_i \bar{\omega}_i(\mathbf{x}), \tag{29}$$

where $\bar{\omega}_i(\mathbf{x}) = \bar{\omega}(\mathbf{x}, \mathbf{x}_i, \boldsymbol{\delta}_i, \boldsymbol{\beta}_i)$, i.e., the C^∞ basis functions at each node are characterized by a vector $\boldsymbol{\delta}_i = (\delta_{i,1}, \ldots, \delta_{i,n})$ that modulates the shape of the rectangular region of influence, and by a vector $\boldsymbol{\beta}_i = (\beta_{i,1}, \ldots, \beta_{i,n})$ of localization exponents along each of the coordinate axes. C^∞ interpolation on an n-dimensional nonuniform grid therefore admits $2nN$ degrees of freedom corresponding to the values of the entries of these two vectors at each node. In this case too, the interpolation scheme can be recast in the form of a linear system,

$$\mathbf{a} = -\boldsymbol{\Omega}^{(\text{nu})}\mathbf{a} + \psi = L^{(\text{nu})}[\mathbf{a}], \tag{30}$$

where $\boldsymbol{\Omega}^{(\text{nu})} = (\Omega^{(\text{nu})}_{(i_1,\ldots,i_n)(j_1,\ldots,j_n)})$ is a $N \times N$ matrix, where the indices refer to the grid nodes. The counterpart of Theorem 2 for nonuniform grids is the following.

THEOREM 3. *Let $\{\mathbf{x}_i\}_{i=1}^N$ be an n-dimensional grid $\{\mathbf{x}_i\}_{i=1}^N$ to which the values $\{\psi_i\}_{i=1}^N$ of a scalar field are assigned. For any choice of $\{\boldsymbol{\delta}_i\}_{i=1}^N$ such that $\delta_{i,j} > 0,\ j = 1, \ldots, n$, there exist positive integers $\beta^*_{i,j} = \beta^*_{i,j}(\{\mathbf{x}_i\})$ that depend on the grid, such that for $\beta_{i,j} > \beta^*_{i,j}$ the operator $L^{(nu)}$ defined by Eq.* (30) *is contractive and the corresponding C^∞ interpolation scheme admits a unique solution.*

Proof. For any node i, there exist $N_i \leq N$ nonzero entries of $\boldsymbol{\Omega}^{(\text{nu})}$ corresponding to the nodes contributing to the interpolation of node i. Let $J(i) = \{j_1(i), \ldots, j_{N_i}(i)\}$ be the indices of these nodes. The sum over the row of the matrix $\boldsymbol{\Omega}^{(\text{nu})}$ for a generic i yields

$$\sum_{j=1}^{N} \left|\Omega_{i,j}^{(\mathrm{nu})}\right| = \sum_{k=1}^{N_i} \left[\prod_{h=1}^{n} \exp\left(-\frac{\beta_{j_k(i),h}\left(x_{i,h} - x_{j_k(i),h}\right)^2}{\delta_{j_k(i),h}^2 - \left(x_{i,h} - x_{j_k(i),h}\right)^2}\right)\right]. \tag{31}$$

Let

$$\beta_{j,h} = \beta \left[\max_{i=1,\ldots,N,\, j\in J(i)} \frac{\delta_{j_k(i),h}^2 - \left(x_{i,h} - x_{j_k(i),h}\right)^2}{\left(x_{i,h} - x_{j_k(i),h}\right)^2}\right]. \tag{32}$$

Eq. (32) leads to the following upper bound for any i:

$$\sum_{j=1}^{N} \left|\Omega_{i,j}^{(\mathrm{nu})}\right| \le \exp(-n\beta)\, N_i. \tag{33}$$

Therefore, by taking $\beta > \max_i \log N_i / n$, the contractivity condition Eq. (23) is fulfilled. ■

IV. NUMERICAL EXAMPLES AND ACCURACY

As a case study to develop general observations on the method proposed and compare it with existing ones, we shall consider the test function on [0, 1],

$$\psi^{(1)}(x) = \frac{x\,(1-x)}{2} - \sin(2\pi x) + \frac{\sin(8\pi x)}{4} + \frac{\sin(16\pi x)}{16}, \tag{34}$$

introduced by Vasilyev *et al.* [17] as a benchmark for interpolation due to its possession of multiple scales.

Since we are interested in C^k functions with $k \ge 0$, it is convenient to make use of the metrics adopted for C^0 functions,

$$d(\psi, \psi_{\mathrm{in}}) = \max_{x\in[0,1]} |\psi(x) - \psi_{\mathrm{in}}(x)|, \tag{35}$$

which is conceptually analogous to the metrics, Eq. (22), of $\Re_\infty^N$. The distance between the derivatives $\psi'(x)$ and $\psi'_{\mathrm{in}}(x)$ can be defined in similar fashion.

Before addressing the accuracy of C^∞ interpolation, let us introduce a modification of external flat interpolation (Case III) in order to account for the differential behavior of the function near the boundaries.

In order to improve the behavior of the interpolation close to the endpoints, we can introduce $2N_e$ external nodes close to $i = 0$ and $i = N$ and extrapolate the behavior of $\psi(x)$ at these nodes from the incremental ratio at the endpoints, i.e., from the discretized two-point representation of the first-order derivative at $x = 0$ and $x = 1$. This corresponds to the assumption that for $x = 0$ and $x = 1$, the extrapolation is linear and given by

$$\begin{aligned} \psi(x) &= \psi(0) - \psi'(x)|_{x=0}\, x, \quad \text{for } x \text{ close to } 0 \\ \psi(x) &= \psi(1) + \psi'(x)|_{x=1}\, (x-1), \quad \text{for } x \text{ close to } 1. \end{aligned} \tag{36}$$

The values of the derivative at the edges can be approximated by applying a two-point differentiation:

$$\begin{aligned} \psi_{-i} &= \psi_0 - (\psi_1 - \psi_0) i, \\ \psi_{N+1} &= \psi_N + (\psi_N - \psi_{N-1}) i, \quad i = 1, \ldots, N_e. \end{aligned} \tag{37}$$

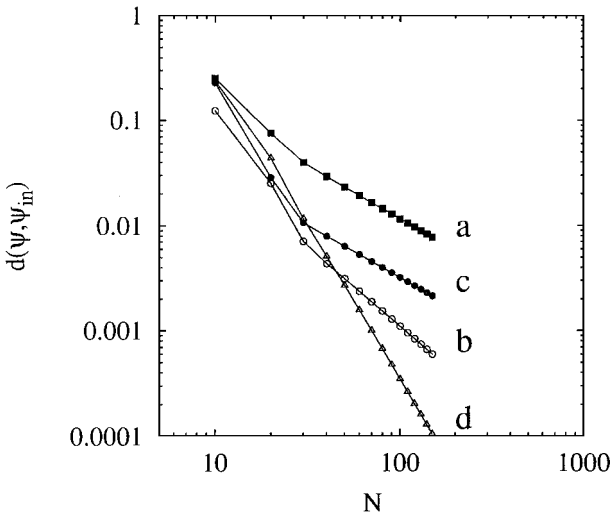

FIG. 3. Behavior of $d(\psi, \psi_{\text{in}})$ vs N for $\psi = \psi^{(1)}$. Eq. (34): (a) piecewise linear; (b) normal cubic splines; (c) C^∞ external flat ($\beta = 30,\ M = 5$); (d) C^∞ with pseudo C^1 continuation ($\beta = 30$, $M = 5$, $N_e = 5$).

Correspondingly, the interpolation scheme is defined for $i = N + 1 + 2\,N_e$ nodes. The external flat interpolation described in Section 3 can be applied to this interpolation scheme. This approach, referred to as pseudo C^1 extension (or continuation), leads to an algebraic structure identical to that of the flat interpolation scheme Eq. (20).

Figure 3 shows the scaling of $d(\psi, \psi_{\text{in}})$ vs the number of interpolation points in the case of C^∞ flat external interpolation and of pseudo C^1 extension compared to that of classical interpolation algorithms (C^0 piecewise linear interpolation and normal cubic splines) for the test function Eq. (34). The numerical results indicate that, with the improvement of the pseudo C^1 continuation, the C^∞ interpolation is more accurate (where accuracy is referred to the uniform norm Eq. (35)) than other methods, including normal cubic splines and straight flat external interpolation. Both normal cubic splines and flat C^∞ interpolation induce a significant error essentially located close to $x = 0$ and $x = 1$, which either does not decrease or decreases more slowly with the number of interpolation points. This phenomenon is evident from the analysis of the derivatives (Fig. 4). C^∞ interpolation with pseudo C^1 extension shows that the error decreases significantly with N.

The results of Figs. 3 and 4 refer to a fixed value of the localization parameter β and of M characterizing the class of compactly supported basis functions Eq. (3). The influence of these parameters on the accuracy of the interpolation is shown in Fig. 5, which illustrates the behavior of the uniform metrics vs $(\beta - \beta^*)/\beta^*$ for several values of M. For external interpolation with pseudo C^1 continuation, accuracy does not depend significantly on M (for $M > 1$). At the same time, however, the value of the localization exponent β should be carefully chosen to be close to the critical values β^* to ensure contractiveness.

To conclude, C^∞ interpolation provides satisfactory results compared to classical interpolation algorithms (such as normal cubic splines). The analysis of the two-dimensional case is addressed in Section V in connection with a physically interesting example related to mixing and Lagrangian chaos.

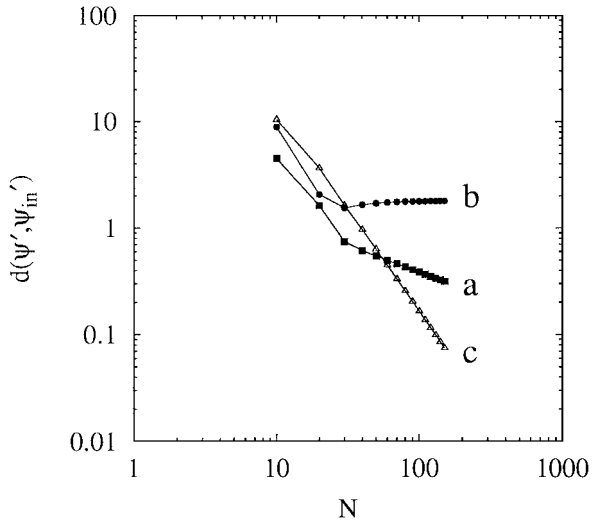

FIG. 4. Behavior of $d(\psi', \psi'_{\text{in}})$ for $\psi = \psi^{(1)}$. Eq. (34): (a) normal cubic splines; (b) flat external C^∞; (c) C^∞ with pseudo C^1 continuation ($\beta = 30,\ M = 5,\ N_e = 5$).

V. INTERPOLATION OF VELOCITY FIELDS THAT GENERATE LAGRANGIAN CHAOS

The Lagrangian characterization of mixing performance associated with a given flow field, say $\mathbf{v}(\mathbf{x}, t)$ ($\mathbf{v}$ being the instantaneous velocity at a generic position $\mathbf{x}$ of the mixing space $\mathcal{M}$), is one field of application of interpolation theory for which the choice of the interpolation strategy is of the utmost importance. Lagrangian analysis involves the determination of geometric and statistical properties associated with the solutions of

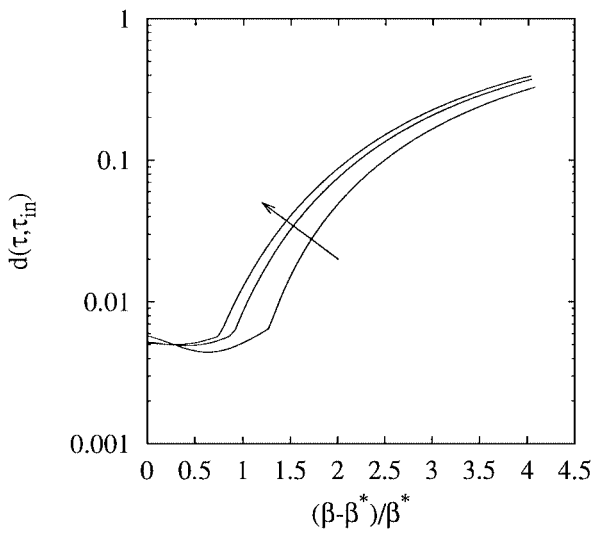

FIG. 5. Behavior of $d(\psi, \psi_{\text{in}})$ vs $(\beta - \beta^*)/\beta^*$ for $\psi = \psi^{(1)}$. Eq. (34) with $N = 40$ for C^∞ interpolation with pseudo C^1 continuation ($N_e = 5$) and $M = 3, 5, 8$. The arrow indicates increasing values of M.

the ODE

$$\dot{\mathbf{x}} = \mathbf{v}(\mathbf{x}, t). \tag{38}$$

While an improved understanding of convective mixing mechanisms has been derived from the application of this approach to simple flows, i.e., flows for which $\mathbf{v}$ is known analytically, in real-world situations the solution of the Navier–Stokes boundary value problem is obtained in a discretized form. The discretization can be performed either in physical space (using finite difference or finite volume techniques) or in a functional space (using finite element or spectral methods). In any case, the outcome of the numerical solution is represented by a set of vector velocities at the nodal positions of a regular or an irregular grid embedded in the flow domain.[4] In order to integrate Eq. (38), the set of nodal velocities must therefore be interpolated so as to continue $\mathbf{v}$ to any point of $\mathcal{M}$.

Souvaliotis *et al.* [23] analyze the numerical issues associated with the solution of the kinematic equation of motion, focusing mainly on the effects of the integration algorithms (i.e., on the discretization, time-integration, and round-off errors intrinsic to any numerical ODE-solver algorithm), on particle trajectories, on the localization of periodic points, and on the scaling of the length of a material filament with time in a two-dimensional periodically forced flow (flow between two eccentric cylinders).

In this section, we address yet another source of error in performing the Lagrangian analysis, namely the impact of different interpolation strategies on the principal kinematic quantities that are commonly used to assess mixing performance.

A. Lagrangian Analysis and Model Flow

The Lagrangian approach to mixing can be dated back to the work by Aref [24], who first highlighted the possibility of obtaining efficient convective mixing within a seemingly simple 2D flow. This author also provided numerical evidence to support the idea that efficient mixing protocols are always associated with chaotic features of tracer trajectories (i.e., solutions of Eq. (38)) for a set of initial conditions of positive Lebesgue measure.[5] This finding has proved of a general character, as demonstrated in a series of computational [25, 26], theoretical [27, 28], and experimental [29, 30] works.

As a result of these studies, it became clear that a Eulerian characterization of mixing through the structural form of the function $\mathbf{v}(\mathbf{x}, t)$ provides only partial insight into mixing performance associated with flow, and that a Lagrangian characterization of mixing cannot

[4] Spectral methods provide a finite dimensional approximation of the solution as a weighted combination of basis functions, so, apparently, there would be no need for interpolation. In most practical cases, however, e.g. in 3D flows, the number of basis functions is on the order of 10^4 or more, making the computational time required to obtain the value of velocity at a single point unacceptable in the context of kinematic analysis. This is due to the fact that, for most of the physically relevant applications of Lagrangian analysis, the integration of the kinematic equations of motion should be performed over long intervals of time and over a statistically significant ensemble of particles (see below for a practical example related to the estimate of the Lyapunov exponent of a chaotic flow). The velocity field can be computed on a discrete set of points and then continued to any point of the flow domain through interpolation of the nodal values.

[5] For two-dimensional flows, this means practically that the chaotic region possesses a finite nonzero "area." The necessity of making use of the Lebesgue measure stems from the phase-space structure of chaotic flows, since periodic points are an invariant set, dense in the chaotic region. Consequently, the simpler Riemann measure is an inadequate tool for approaching the statistical properties of chaotic flows.

be approached in terms of a general solution of Eq. (38), as chaotic systems display sensitive dependence on initial conditions. A set of feasible computational tools that are sufficiently robust for the purposes of numerical investigation is therefore needed in order to establish mixing performance objectively. This set of tools includes the following:

- *Poincaré sections*. This technique applies to time-periodic and spatially periodic flows (more generally speaking, it can be implemented on any flow that admits a global section [31]). In the time-periodic case, it consists of superimposing onto a single plot all the positions occupied by a generic particle at multiple integers of the flow period. In cases where the trajectory is chaotic, its Poincaré section densely fills a subregion of the mixing space with positive measure (chaotic region).
- *Lyapunov exponents*. Poincaré sections yield a primarily qualitative characterization of chaos, providing an overall picture of the number and shape of the chaotic regions associated with a given mixing protocol. A more quantitative but still global measure of the "amount of chaos" within each of the chaotic regions is achieved through computation of the Lyapunov exponents, which yield the average rate of stretching experienced by an infinitesimal vector attached to a chaotic orbit $\mathbf{x}(t)$. In quantitative terms, Lyapunov exponents are defined as

$$\lim_{t\to\infty} \frac{1}{t} \ln \lambda(t), \tag{39}$$

where the *stretching* $\lambda(t)$ is defined as $\lambda(t) = \|\mathbf{l}(t)\|, \mathbf{l}(t) = (l_1(t), \ldots, l_n(t))^T$ being the solution of the ODE system

$$\frac{dl_i}{dt} = \sum_{j=1}^{n} \left.\frac{\partial v_i}{\partial x_j}\right|_{\mathbf{x}(t),t} l_j, \quad \|\mathbf{l}(0)\| = 1. \tag{40}$$

For an n-dimensional flow, there are at most n different values, $\Lambda_1, \ldots, \Lambda_n$, of the limit in Eq. (39) [31], albeit for almost all the values of $\mathbf{l}(0)$ (with the exception of a set of zero measure), the quantity Eq. (39) converges towards the maximum Lyapunov exponent of the system Λ, which is the maximum of $\Lambda_i, i = \mathbf{1}, \ldots, n$. Most importantly, the set of Lyapunov exponents is independent of the initial condition $\mathbf{x}(0)$ whenever $\mathbf{x}(0)$ is chosen within one and the same chaotic region.

- *Stretching distributions and short-time Lyapunov exponents*. As they are the result of long-time averaging, Lyapunov exponents cannot account for the heterogeneity of stretching events. A statistical measure of this aspect of micromixing is provided by the PDF, $\mathcal{F}(\ln(\lambda(t)))$, of the values $\ln \lambda(t)$ of stretching experienced by a population of vectors attached to N points distributed within the mixing space. If the N vectors are embedded within a single chaotic region, $\mathcal{C}$, then the mean $\langle \ln \lambda(t) \rangle_{\mathcal{F}}$ scales as Λt, where Λ is the largest Lyapunov exponent associated with $\mathcal{C}$. Analogous computations can be performed by using the ratio $\ln \lambda(t)/t$ (short-time Lyapunov exponent) instead of $\ln \lambda(t)$. In this case, the PDF tends toward a Dirac's delta function centered at Λt.
- *Line and surface tracking*. Lagrangian tracking of material lines and surfaces (representing the interface between segregated regions in 2D and 3D, respectively) that are passively advected by the flow provides a geometric characterization of the evolution of partially mixed structures. In the presence of chaos, passive interfaces undergo a space-filling dynamics that is independent of the initial shape and size of the segregated regions. The characterization of the invariant properties of passive interfaces is of great interest

in modeling the dynamics of chemical reactions and of heat transfer processes that occur along with chaotic advection [35, 36]. Most importantly for our purposes, interface tracking constitutes a severe test of interpolation schemes.

In the remainder of this section, we use a two-dimensional time-periodic model flow to compare the influence of interpolation on Poincaré sections, Lyapunov exponents, and evolutes of material lines that are passively advected by the mixing protocol.

The time-periodic flow is obtained by blinking every $T/2$ time units two steady fields $\mathbf{v}_1$ and $\mathbf{v}_2$, where $\mathbf{v}_1$ and $\mathbf{v}_2$ are defined through their stream functions

$$\psi^{(1)}(x, y) = \psi(x, y) = \sin^2(\pi x)\, \sin(\pi y^2) \tag{41}$$

and

$$\psi^{(2)}(x, y) = \psi(x, 1 - y), \tag{42}$$

where $\psi^{(1)}$, $\psi^{(2)}$ are defined on the unit box $0 \leq x \leq 1$, $0 \leq y \leq 1$. Each $\mathbf{v}_i = \mathbf{v}^{(i)}(\mathbf{x}) = (\partial\psi^{(i)}/\partial y - \partial\psi^{(i)}/\partial x)^T$ $(i = 1, 2)$ is therefore by definition an incompressible flow. The assumption of instantaneous switching, rigorously verified in creeping-flow regimes, is a reasonable approximation at low Reynolds numbers (see [37] for a discussion of this subject). Although the stream function ψ is a solution of neither the Navier–Stokes nor the Stokes equation, it yields qualitatively similar behavior to that of a physically realizable driven cavity flow,[6] as far as global properties associated with the kinematics of tracer and inertial particles are concerned.

The stream function Eq. (41) originates a velocity field with vanishing normal and tangential velocity components at the boundary of the cavity, with the exception of the wall at $y = 1$, where v_x is different from zero. This model flow, which is referred to here as prototypical cavity flow (PCF), depends on a single parameter, namely the half period of motion T. In presenting simulation results, we focus on the protocol $T = 0.3$, which gives rise to a main region of chaotic motion intertwined with islands of quasiperiodicity. The numerical integration of the kinematic equations is performed by applying a Runge–Kutta fourth-order method.

B. Effects of Interpolation

In order to analyze the accuracy of C^∞ interpolation and its effects on the Lagrangian analysis of chaotic flows, it is useful to make a quantitative comparison with the classical interpolation schemes most commonly used for fluid dynamics problems.

There are essentially three main approaches:

1. Piecewise linear interpolation. Starting from a triangulation of the mixing space $\mathcal{M}$, the velocity field is expressed as a linear function of the local (barycentric) coordinates within each element (triangles in two dimensions, tetrahedrons in three). This is the simplest approach to interpolation and finds application especially in connection with finite-element simulations. Piecewise linear interpolation yields a globally continuous, piecewise smooth interpolated function.

[6] The main difference with respect to classical cavity flow is that this model possesses no singularities at the corners of the cavity.

TABLE I
Interpolation Accuracy Referred to the Uniform Distance Eq. (35) for Several Two-Dimensional Fields[a]

		Linear C^0	Bilinear	C^∞
$N = 10$	ψ	$5.74 \cdot 10^{-2}$	$5.00 \cdot 10^{-2}$	$1.48 \cdot 10^{-2}$
	v_x	$3.72 \cdot 10^{-1}$	$3.35 \cdot 10^{-1}$	$1.70 \cdot 10^{-1}$
	v_y	$2.93 \cdot 10^{-1}$	$2.36 \cdot 10^{-1}$	$3.22 \cdot 10^{-2}$
$N = 30$	ψ	$6.74 \cdot 10^{-3}$	$6.0 \cdot 10^{-3}$	$1.63 \cdot 10^{-3}$
	v_x	$4.88 \cdot 10^{-2}$	$4.75 \cdot 10^{-2}$	$2.36 \cdot 10^{-2}$
	v_y	$4.75 \cdot 10^{-2}$	$2.70 \cdot 10^{-2}$	$2.67 \cdot 10^{-3}$

[a] $\psi(x, y)$, $v_x(x, y)$, $v_y(x, y)$ associated with PCF flow for linear, bilinear, and C^∞ interpolation ($M = 3$, $\beta = 25$, $N_e = 3$).

2. Bilinear interpolation. It is applied for square grids and is the most common method in many applications. To quote Press *et al.* [4], bilinear interpolation is "frequently close enough for government work."

3. Bicubic interpolation. Both piecewise linear and bilinear interpolation yield a continuous interpolating function for a generic field $\psi(x, y)$ that possesses discontinuous partial derivatives at the boundary between adjacent discretization elements. Bicubic interpolation returns a C^1 interpolating function and requires the specification at each node of the values of the gradient, i.e., of $\partial\psi/\partial x$, $\partial\psi/\partial y$, and of the second-order cross derivative $\partial^2\psi/\partial x\partial y$. This is a significant drawback, as the accuracy of the interpolation depends essentially on the accuracy of the values of these first- and second-order derivatives.[7] Due to its intrinsic arbitrariness, this method is not explicitly considered here.

We focus on the accuracy properties for a comparatively small number of grid points per coordinate axis ($N = 10 \div 30$), corresponding to $(N + 1)^2$ overall grid points, since this is the most critical case frequently encountered in applications.

Let us first consider the accuracy of the interpolation scheme expressed in terms of uniform distance between the exact and the interpolated field over the unit square. Table 1 gives the results for the piecewise linear, bilinear, and C^∞ interpolation (with pseudo C^1 continuation) of the function $\psi(x, y)$, $v_x(x, y)$, $v_y(x, y)$ for $N = 10$ and 30 grid points per coordinate axis. C^∞ interpolation with pseudo C^1 continuation gives better results than the other methods considered. The two components of the velocity field obtained from the C^∞ interpolation algorithms are shown in Fig. 6.

The quantitative characterization of accuracy in interpolating the velocity field provides only partial validation of an interpolation method when applied within a Lagrangian framework. Results deriving from Lagrangian analysis are affected by integral errors corresponding to the accumulation of the interpolation error along a particle trajectory, on which integration errors are unavoidably numerically superimposed.

As an initial check on the accuracy of an interpolation scheme for Lagrangian analysis, we shall consider the asymptotic behavior of a particle trajectory starting from a point belonging to a chaotic region $\mathcal{C}$. Since the velocity field is a periodic function of time, we

[7] Indeed, in the case of stream-function interpolation, assigning the first-order derivatives $\partial\psi/\partial y$, $-\partial\psi/\partial x$ of the stream function is equivalent to specifying the velocity field at grid nodes, which is instead one of the purposes of the interpolation.

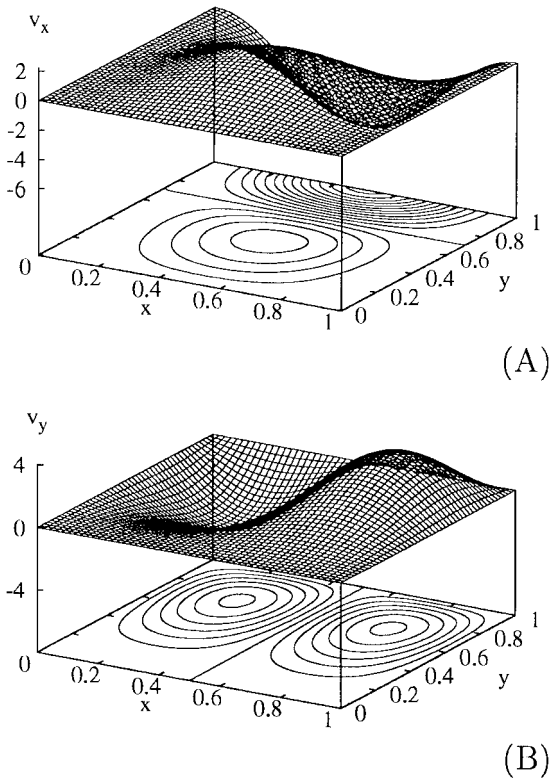

FIG. 6. Reconstruction of the velocity field of PCF flow using C^∞ interpolation with pseudo C^1 continuation ($M = 3$, $\beta = 25$, $N_e = 3$). (A) $v_x(x, y)$. (B) $v_y(x, y)$.

can consider a stroboscopic representation expressed by a Poincaré map Φ, $\mathbf{x}_{n+1} = \Phi(\mathbf{x}_n)$, where $\mathbf{x}_n = \mathbf{x}(n\,T_p)$.

The numerical experiment is performed as follows: we pick an initial point $\mathbf{x}_0 \in \mathcal{C}$ belonging to a chaotic region and consider a segment of the (discrete) trajectory for a sufficiently large number of iterations N_{as}, with N_{as} of the order $5 \cdot 10^4$. After this transient, the asymptotic behavior of the trajectory is analyzed. Figure 7 shows a comparison of asymptotic behavior for several interpolation schemes for the PCF flow at $T = 0.3$ for $N = 10$. Piecewise linear interpolation yields trajectories that become attracted to one of the walls after a short transient. The same situation occurs for bilinear interpolation, as shown in Fig. 7A obtained after a transient of $N_{\text{as}} = 4 \cdot 10^4$ iterations. As can be observed, the trajectory wanders throughout the chaotic region (compare Figs. 7A and 7C) before collapsing at the wall point. This means that C^0 interpolations introduce significant and structural errors. The asymptotic behavior of a chaotic trajectory becomes attracted by a limit set, represented in this case by a single point. This behavior is clearly a numerical artifact, as it is physically inconsistent with flow incompressibility. This means that for a coarse grid, C^0 interpolations are unable to preserve the invariance property of the chaotic region, and superimposition of interpolation and integration errors causes Eq. (38) to behave like a dissipative system.

Conversely, C^∞ interpolation (Fig. 7B) yields an asymptotic global picture of the chaotic region that closely resembles the result deriving from the integration of the exact velocity field (Fig. 7C).

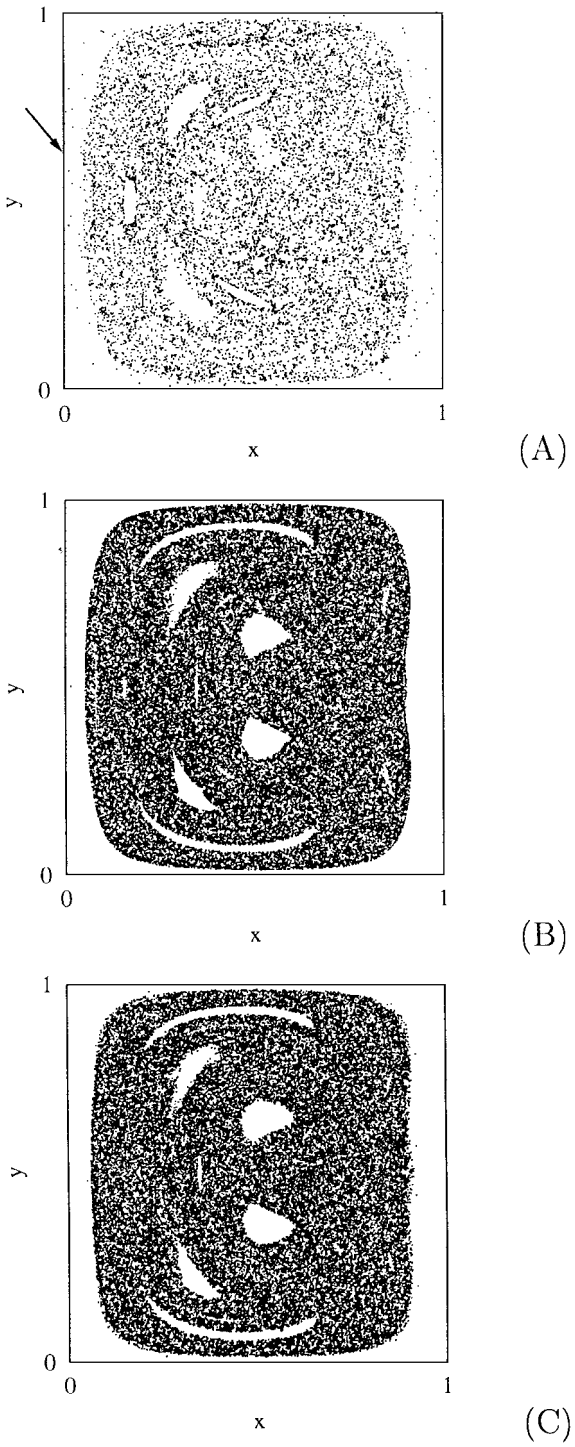

FIG. 7. Stroboscopic trajectory of a point belonging to the chaotic region for different interpolations of the velocity field for PCF flow ($T = 0.30$) with $N = 10$. (A) Bilinear interpolation ($N_{as} = 4 \cdot 10^4$). The arrow indicates the limit point of the trajectory. (B) C^∞ interpolation with pseudo C^1 continuation ($M = 3$, $\beta = 25$, $N_e = 3$, $N_{as} = 5 \cdot 10^4$). (C) Exact velocity field.

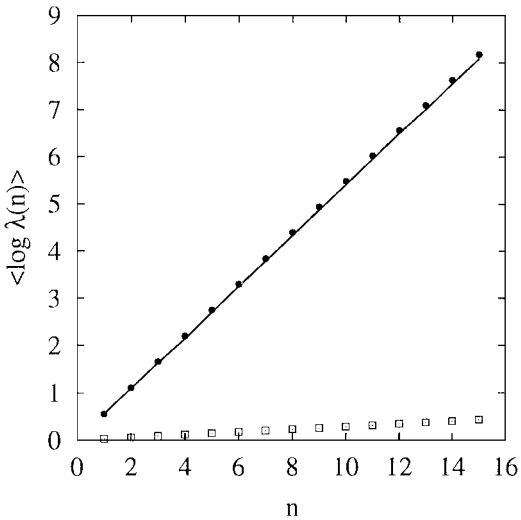

FIG. 8. Scaling of $\langle \log \lambda(n) \rangle$ vs n for the PCF flow ($T = 0.30$) for $N = 10$. Continuous line: results deriving from the exact velocity field. (⊡) Bilinear interpolation. (●) C^∞ interpolation with pseudo C^1 continuation ($M = 3$, $\beta = 25$, $N_e = 3$).

This semiqualitative observation is corroborated by analysis of the scaling of the Lyapunov exponents. In the present (two-dimensional) case, the spectrum of Lyapunov exponents associated with a generic trajectory is of the type $\{-\Lambda, \Lambda\}$, with $\Lambda > 0$ if the orbit is chaotic.[8]

Figure 8 shows the behavior of $\langle \log \lambda(n) \rangle$ vs n for $T = 0.3$ for several interpolation schemes. Given that the flow is time-periodic, the stretching exponent is computed from its Poincaré map,

$$\langle \log \lambda(n) \rangle = \frac{1}{N_s} \sum_{i=1}^{N_s} \log \| \Phi^{n*}(\mathbf{x}_i)\mathbf{v} \| \sim \Lambda n, \tag{43}$$

where $\Phi^{n*}(\mathbf{x}) = \partial \Phi^n(\mathbf{x})/\partial \mathbf{x}$ is the Jacobian matrix of the n-th iterative Φ^n of the Poincaré map Φ, $\mathbf{v}$ is a generic unit vector, and N_s indicates the number of averages along the trajectory. Eq. (43) enables us to compute the Lyapunov exponent Λ (referred to the Poincaré map) from the linear scaling with time n of the stretching exponents.[9]

Simulation results are obtained by averaging $N_s = 10^4$ points along a trajectory, after a transient of $N_{\text{as}} = 4 \cdot 10^4$ iterations. The starting point is the same for all the simulations.

As can be observed, C^∞ interpolation provides a time behavior of the stretching exponents that is very close to that obtained from the integration of the exact velocity field, while bilinear interpolation fails to predict the scaling Eq. (43) due to the fact that the trajectory collapses towards a limit point at the boundary. The occurrence of a weakly positive Lyapunov exponent obtained from bilinear interpolation depends on the choice of the initial transient $N_{\text{as}} = 4 \cdot 10^4$ iterations. As can be observed from Fig. 7A, the trajectory remains for some time within the chaotic region before collapsing towards the limit point.

[8] The Lyapunov spectrum structure follows from the fact that the flow is measure-preserving. This means that $\sum_{i=1}^{i=n} \Lambda_i = 0$ [32].

[9] The Lyapunov exponent of the time-continuous system is given by $\Lambda/2T$.

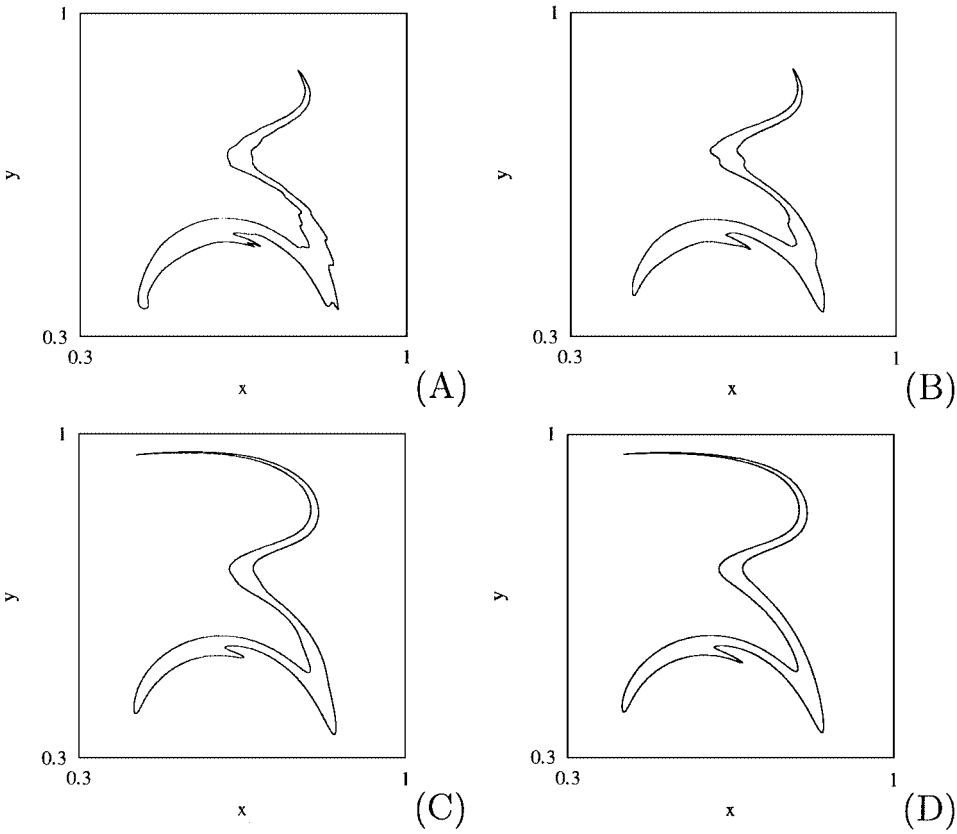

FIG. 9. Evolution of a material filament after $n = 2$ iterations of the Poincaré map associated with the PCF flow at $T = 0.30$. (A) Linear interpolation. (B) Bilinear interpolation. (C) C^∞ interpolation with pseudo C^1 continuation ($M = 3$, $\beta = 25$, $N_e = 3$). (D) Exact velocity field.

The clash of linear and bilinear interpolation depends of course on the coarse discretization that was adopted ($N = 10$) in order to test the "Lagrangian accuracy" of interpolation schemes in a critical case.

As a further test on interpolation performance, we consider the dynamics of partially mixed structures. In 2D systems, this means determining the evolution of a generic closed line. The tracking of material lines makes it possible to uncover the underlying invariant geometry that characterizes laminar chaotic flows, namely the global unstable foliation associated with the chaotic region. In the limit of vanishing diffusivity, this geometric object behaves like an attractor [35, 36] for passively advected interfaces. In this case, the difference between C^0 and C^∞ interpolation is striking, since the first fails to preserve the smoothness of evoluted interfaces as a result of derivative discontinuities across the cell boundaries.

This phenomenon is clearly shown in Figs. 9 and 10, which show the evolute after $n = 2$ periods (i.e., at a time $t = 2T$) of a circumference of radius $\varepsilon = 10^{-1}$ centered at $(0.7, 0.5)$. A coarse grid ($N = 10$) was purposely chosen to highlight differences among the interpolation schemes. C^0 interpolation schemes, both linear and bilinear, fail to reproduce the evolution of a material line as from the early stages of the mixing process (Figs. 9A and 9B and 10A and 10B compared to Figs. 9D and 10D). Conversely, interpolation schemes that are globally differentiable (and, *a fortiori*, C^∞) yield a geometrical representation of

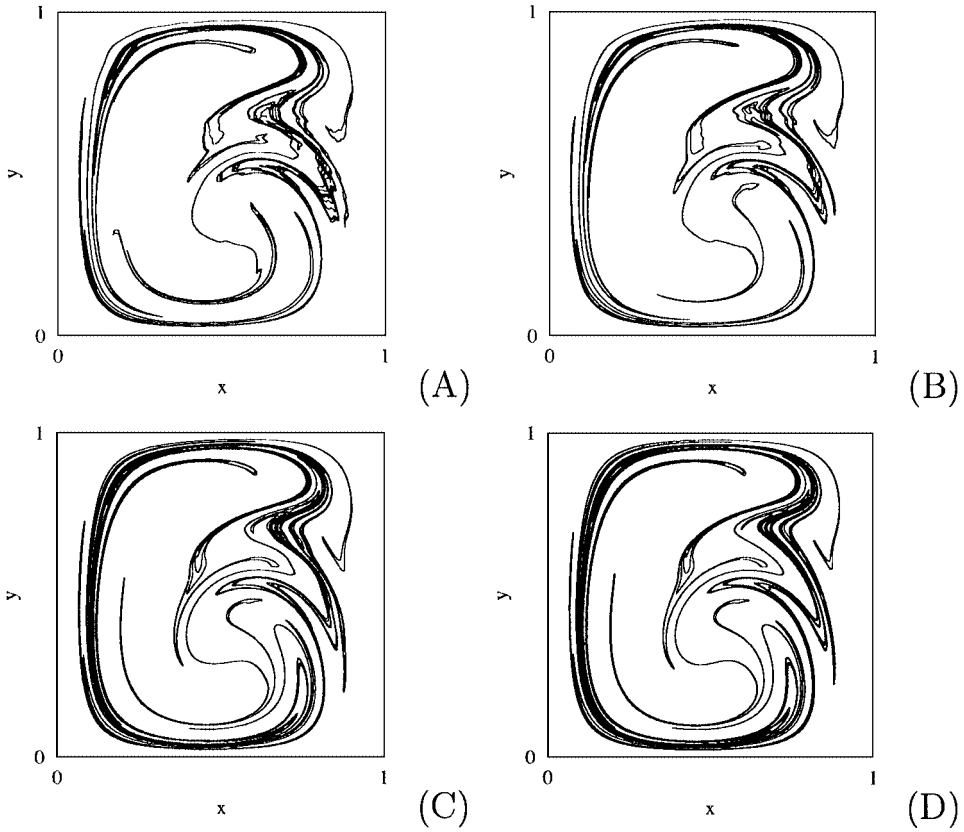

FIG. 10. Evolution of a material filament after $n = 6$ iterations of the Poincaré map associated with the PCF flow at $T = 0.30$. (A) Linear interpolation. (B) Bilinear interpolation. (C) C^∞ interpolation with pseudo C^1 continuation ($M = 3$, $\beta = 25$, $N_e = 3$). (D) Exact velocity field.

partially mixed structures that is fairly close to that obtained from the exact velocity field (compare Figs. 9C and 9D and 10C and 10D).

It should also be mentioned that C^0 interpolation schemes prevent the analysis of higher-order geometric properties such as local interface curvature, which has proved useful in characterizing chaotic dynamics in general [33], and bubble breakup and coalescence phenomena in particular [34].

The result derived in this section for the evolution of passively advected interfaces starting from an interpolated velocity field over a coarse grid is analogous to what occurs in the case of inertial particles moving by viscous drag [39] within a two- or three-dimensional chaotic flow [40, 41]. The application of coarse C^0 interpolation was shown to produce a distorted picture of the limit attractor, qualitatively analogous to what is observed for passive interfaces in Figs. 9 and 10.

V. CONCLUDING REMARKS

The introduction of C^∞ interpolation is designed to provide a simple interpolation scheme with arbitrary regularity. The regularity issue is often overlooked, but can be of paramount importance in many problems related to first- and second-order differential properties

obtained from the solution of ordinary or partial differential equations involving interpolated fields.

From a practical point of view, the property of compact support of the interpolation basis functions ensures that estimation of the field at any point involves solely the contribution of the basis functions falling within a prescribed region of influence. This means that the value of the interpolated function is obtained by summing over a number of basis functions that is much smaller than the total number of grid points.

Theorems 1–3 ensure the applicability of this interpolation scheme and provide a simple and computationally straightforward iterative way to obtain the interpolation coefficients starting from an arbitrary initial choice, as a result of the contractive nature of the linear operator associated with the interpolation scheme.

Within the manifold of possible applications, fluid dynamics problems (e.g., Lagrangian analysis of particle motion and mixing performances) appear to be the natural domain of application of this interpolation technique. More generally speaking, the interpolation scheme proposed may prove a better choice than other classical methods whenever the regularity of the interpolating function plays a role.

C^∞ interpolation applies to a discrete representation of scalar and vector fields. Due to the compactness of the support of the basis functions, it can be used in the context of meshless (e.g., spectral) methods, in order to reduce the computational burden associated with the pointwise evaluation of the field, starting from a generalized Fourier expansion involving many ($\sim 10^4 \div 10^5$) modes.

Lagrangian analysis provides a significant benchmark by highlighting defects of interpolation methods that would be difficult to observe in Eulerian simulations.

It may be useful to mention in passing that as the expansion with respect to the basis $\omega(x; x_i, \delta, \beta)$, Eq. (8), can be applied to develop efficient compactly supported collocation methods for solving partial differential equations, conceptually analogous to wavelet collocations, and for approaching gauge theories of fluid dynamics, i.e., obtaining the potential functions associated with the poloidal–toroidal decomposition of an incompressible three-dimensional velocity field starting from a discretized knowledge of it. This issue will be discussed in detail elsewhere.

REFERENCES

1. J. H. Ferziger and M. Peric, *Computational Methods for Fluid Dynamics* (Springer-Verlag, Berlin, 1996).
2. P. K. Yeung and S. B. Pope, An algorithm for tracking fluid particles in numerical simulations of homogeneous turbulence, *J. Comput. Phys.* **79**, 373 (1988).
3. P. J. Roache, *Computational Fluid Dynamics* (Hermosa, Albuquerque, NM, 1985).
4. W. H. Press, S. A. Teukolsky, W. T. Vetterling, and B. P. Flannery, *Numerical Recipes in Fortran—The Art of Scientific Publishing*, 2nd ed. (Cambridge Univ. Press, Cambridge, UK, 1992).
5. W. S. Russell, Polynomial interpolation schemes for internal derivative distributions on structured grids, *Appl. Numer. Math.* **17**, 129 (1995).
6. J. W. Deardorff and R. L. Peskin, Lagrangian statistics from numerically integrated turbulent shear flow, *Phys. Fluids* **13**, 584 (1970).
7. P. K. Yeung and S. B. Pope, Lagrangian statistics from direct numerical simulations of isotropic turbulence, *J. Fluid Mech.* **207**, 531 (1989).
8. J. M. Ottino, *The Kinematics of Mixing: Stretching, Chaos, and Transport* (Cambridge Univ. Press, New York, 1989).

9. M. D. Buhmann, Multivariate cardinal interpolation with radial-basis functions, *Constr. Approx.* **6**, 225 (1990).
10. R. Schaback, Comparison of radial basis function interpolants, in *From CAGD to Wavelets*, edited by K. Jetter and F. Utrera (World Scientific, Singapore, 1993), pp. 293–305.
11. Z.-M. Wu and R. Schaback, Local error estimates for radial basis function interpolation of scattered data, *I.M.A. J. Numer. Anal.* **13**, 13 (1993).
12. G. Cybenko, Approximation by superposition of sigmoidal functions, *Math. Contr. Signals Syst.* **2**, 303 (1989).
13. K. Hornik, M. Stinchcombe, and H. White, Multilayer feedforward networks are universal approximators, *Neur. Net.* **2**, 359 (1989).
14. J. Park and I. W. Sandberg, Universal approximation using radial-basis-function networks, *Neur. Comput.* **3**, 246 (1991).
15. S. Dubuc, Interpolation through an iterative scheme, *J. Math. Anal. Appl.* **114**, 185 (1986).
16. G. Deslauriers and S. Dubuc, Symmetric iterative interpolation schemes, *Constr. Approx.* **5**, 49 (1989).
17. O. V. Vasilyev, S. Paolucci, and M. Sen, A multilevel wavelet collocation method for solving partial differential equations in a finite domain, *J. Comput. Phys.* **120**, 33 (1995).
18. M. Holmström, *Solving Hyperbolic PDEs using Interpolation Wavelets*, Uppsala Univ. Inst. för Teknisk Databehandling, Report 189/1996.
19. C. K. Chui, *An Introduction to Wavelets* (Academic Press, San Diego, 1992).
20. V. S. Vladimirov, *Equations of Mathematical Physics* (Mir, Moscow, 1984).
21. G. H. Golub and C. F. Van Loan, *Matrix Computations* (North Oxford Academic, Oxford, 1983).
22. A. N. Kolmogorov and S. V. Fomin, *Elements of the Theory of Functions and Functional Analysis* (Dover, New York, 1975).
23. A. Souvaliotis, S. C. Jana, and J. M. Ottino, Potentialities and limitations of mixing simulations, *AIChE J.* **41**, 1605 (1995).
24. H. Aref, Stirring by chaotic advection, *J. Fluid Mech.* **143**, 1 (1984).
25. B. Eckhardt and H. Aref, Integrable and chaotic motions of four vortices. II. Collision dynamics of vortex pairs, *Phil. Trans. R. Soc. Lond. Ser. A* **326**, 655 (1998).
26. F. J. Muzzio, P. D. Swanson, and J. M. Ottino, The statistics of stretching and stirring in chaotic flows, *Phys. Fluids A* **3**, 822 (1991).
27. V. Rom-Kedar, A. Leonard, and S. Wiggins, An analytical study of transport, mixing, and chaos in an unsteady vortical flow, *J. Fluid Mech.* **214**, 347 (1990).
28. D. Beigie, A. Leonard, and S. Wiggins, Invariant manifold templates for chaotic advection, *Chaos, Solitons, and Fractals* **4**, 749 (1994).
29. C. W. Leong and J. M. Ottino, Experiments on mixing due to chaotic advection in a cavity, *J. Fluid Mech.* **209**, 463 (1989).
30. H. A. Kusch and J. M. Ottino, Experimental and computational studies of mixing in complex Stokes flows: The vortex mixing flow and multicellular cavity flows, *J. Fluid Mech.* **269**, 199 (1994).
31. A. Katok and B. Hasselblatt, *Introduction to the Modern Theory of Dynamical Systems* (Cambridge Univ. Press, Cambridge, UK, 1995).
32. J. P. Eckmann and D. Ruelle, Ergodic theory of chaos and strange attractors, *Rev. Modern Phys.* **57**, 617 (1985).
33. S. Cerbelli, J. Zalc, and F. J. Muzzio, The evolution of material lines curvature in deterministic chaotic flows, *Chem. Eng. Sci.* **55**, 363 (2000).
34. M. Tjahjadi and J. M. Ottino, Stretching and breakup of droplets in chaotic flows, *J. Fluid Mech.* **232**, 191 (1991).
35. M. M. Alvarez, F. J. Muzzio, S. Cerbelli, A. Adrover, and M. Giona, Self-similar spatiotemporal structure of intermaterial boundaries in chaotic flows, *Phys. Rev. Lett.* **81**, 3395 (1998).
36. M. Giona, A. Adrover, F. J. Muzzio, S. Cerbelli, and M. M. Alvarez, The geometry of mixing in time-periodic chaotic flows I—Asymptotic directionality in physically realizable flows and global invariant properties, *Physica D* **132**, 298 (1999).

37. M. Liu, R. L. Peskin, and F. J. Muzzio, Structure of the stretching field in chaotic cavity flows, *AIChE J.* **40**, 1273 (1994).
38. M. Giona and A. Adrover, Nonuniform stationary measure of the invariant unstable foliation in Hamiltonian and fluid mixing systems, *Phys. Rev. Lett.* **81**, 3864 (1998).
39. M. R. Maxey and J. J. Riley, Equation of motion for a small rigid sphere in a nonuniform flow, *Phys. Fluids* **26**, 883 (1983).
40. M. Liu, R. L. Peskin, and F. J. Muzzio, Fractal structure of a dissipative particle–fluid system in a time-dependent chaotic flow, *Phys. Rev. E* **50**, 4245 (1994).
41. A. C. Omurtag, P. Dutta, and R. Chevray, Attractors of finite-sized particles: An application to enhanced separation, *Phys. Fluids* **8**, 3212 (1996).